

ARTICLE

<https://doi.org/10.1038/s41467-018-08136-3>

OPEN

Non defect-stabilized thermally stable single-atom catalyst

Rui Lang¹, Wei Xi², Jin-Cheng Liu³, Yi-Tao Cui⁴, Tianbo Li^{1,5}, Adam Fraser Lee⁶, Fang Chen¹, Yang Chen^{1,5}, Lei Li⁷, Lin Li¹, Jian Lin¹, Shu Miao¹, Xiaoyan Liu¹, Ai-Qin Wang¹, Xiaodong Wang¹, Jun Luo², Botao Qiao^{1,8}, Jun Li^{3,9} & Tao Zhang¹

Surface-supported isolated atoms in single-atom catalysts (SACs) are usually stabilized by diverse defects. The fabrication of high-metal-loading and thermally stable SACs remains a formidable challenge due to the difficulty of creating high densities of underpinning stable defects. Here we report that isolated Pt atoms can be stabilized through a strong covalent metal-support interaction (CMSI) that is not associated with support defects, yielding a high-loading and thermally stable SAC by trapping either the already deposited Pt atoms or the PtO₂ units vaporized from nanoparticles during high-temperature calcination. Experimental and computational modeling studies reveal that iron oxide reducibility is crucial to anchor isolated Pt atoms. The resulting high concentrations of single atoms enable specific activities far exceeding those of conventional nanoparticle catalysts. This non defect-stabilization strategy can be extended to non-reducible supports by simply doping with iron oxide, thus paving a new way for constructing high-loading SACs for diverse industrially important catalytic reactions.

¹State Key Laboratory of Catalysis, Dalian Institute of Chemical Physics, Chinese Academy of Sciences, Dalian 116023, China. ²Center for Electron Microscopy and Tianjin Key Lab of Advanced Functional Porous Materials, Institute for New Energy Materials, School of Materials, Tianjin University of Technology, Tianjin 300384, China. ³Department of Chemistry & Key Laboratory of Organic Optoelectronics and Molecular Engineering of the Ministry of Education, Tsinghua University, Beijing 100084, China. ⁴Synchrotron Radiation Laboratory, Laser and Synchrotron Research Center (LASOR), The Institute for Solid State Physics, The University of Tokyo, 1-490-2 Kouto, Shingu-cho Tatsuno, Hyogo 679-5165, Japan. ⁵University of Chinese Academy of Sciences, Beijing 100049, China. ⁶School of Science, Royal Melbourne Institute of Technology University, Melbourne VIC3001, Australia. ⁷Synchrotron Radiation Nanotechnology Center, University of Hyogo, 1-490-2 Kouto, Shingu-cho Tatsuno, Hyogo 679-5165, Japan. ⁸Dalian National Laboratory for Clean Energy, Dalian 116023, China. ⁹Department of Chemistry, Southern University of Science and Technology, Shenzhen 518055, China. These authors contributed equally: Rui Lang, Wei Xi and Jin-Cheng Liu. Correspondence and requests for materials should be addressed to J.L. (email: jluo@tjut.edu.cn) or to B.Q. (email: bqiao@dicp.ac.cn) or to J.L. (email: junli@tsinghua.edu.cn)

Heterogeneous catalysis is pivotal to the modern chemical industry¹, with many heterogeneous catalysts comprising transition metals deposited over a solid support phase². A recent evolution in this field is the dispersion of isolated, individual metal atoms over the support to form single-atom catalysts (SACs)³. Such SACs have attracted considerable attention as a new frontier in heterogeneous catalysis^{4,5}, affording enhanced precious metal thrifing⁶ and atom economy^{7–9}, improved active site homogeneity^{10–12}, and the ability to tune the metal-support interface with unprecedented control^{13–16}, resulting in superior catalytic activity^{17–20} and/or high selectivity^{21–23}. A diverse range of supports are known to stabilize isolated metal atoms, notably through pinning at electronic and/or structural defects associated with coordinatively unsaturated sites (CUS) by experimental and density functional theory (DFT) studies (Supplementary Appendices I and II)^{24–33}. The concentration of atomically-dispersed metal atoms, and their stability, are therefore intrinsically linked to the density and stability of defects as described in recent reviews (Supplementary Appendix III)^{34,35}. However, it is extremely difficult to create a high density of thermally stable support defects³⁶, and hence the fabrication of high metal loading SACs remains currently a formidable challenge.

Here we report the discovery that single metal atoms can be stabilized through a strong covalent metal-support interaction (CMSI) that is not associated with surface defects, enabling the genesis of high concentrations of thermally stable single atoms, even on low-surface-area materials. In situ genesis of ferric oxide supported Pt SAC from Pt nanoparticles (NPs) is verified in methane combustion reaction, one of the primary means of human energy production and important for mitigating environmental challenge associated with CH₄ emission. Experimental and DFT studies demonstrate that metal oxide reducibility dictates the ability of a support to anchor isolated Pt atoms: α -Fe₂O₃ favors atomically dispersed Pt, whereas Al₂O₃ favors NP sintering. However, the non defect-stabilization strategy can be extended to non-reducible oxide by simply doping with iron oxide. This finding provides a promising method to fabricate high-metal-loading SACs with excellent thermal stability.

Results

Co-precipitation prepared thermally stable Pt₁/FeO_x. A 1.8 wt% Pt/FeO_x catalyst was first prepared by co-precipitation (the synthesis details are in the Methods section), denoted as Pt₁/FeO_x, and subsequently calcined at 800 °C in air for 5 h, denoted as Pt₁/FeO_x-C800. Aberration-corrected high-angle annular dark-field scanning transmission electron microscopy (AC-HAADF-STEM) with sub-angstrom resolution was used to compare the nature of platinum species between these two materials. In neither case were Pt nanoclusters or NPs observed (Supplementary Figures 1 and 2). Pt₁/FeO_x comprised isolated Pt atoms dispersed on the FeO_x support with some Pt atoms exactly aligned with the Fe atomic columns (Fig. 1a–b). Corresponding CO diffuse reflectance infrared Fourier transform spectroscopy (DRIFTS) of Pt₁/FeO_x (Supplementary Figure 1c) shows a coverage-independent band at ~2089 cm⁻¹ and the absence of bridged adsorption of CO band (~1860 cm⁻¹), which is consistent with the CO linearly bound to isolated Pt atoms³. Note that our CO infrared bands are broader than those recently reported by Christopher and co-workers³⁷. However, this is unsurprising because in their work ultra-dilute (0.05 wt%) Pt loadings were used to immobilize only one Pt atom per 5 nm monodispersed anatase nanocrystal. Such low loadings favor the population of only the most reactive titania surface sites, and hence a homogeneous local environment. Platinum sintering was not observed following 800 °C calcination by either AC-HAADF-STEM

(Fig. 1c–d and Supplementary Figure 2a–b), or powder X-ray diffraction (Supplementary Figure 2c) analysis of the Pt₁/FeO_x-C800 sample. X-ray absorption spectroscopy (XAS) studies provide further evidence for the complete dispersion of Pt atoms. Figure 1e presents the Fourier transform radial distribution functions of *k*³-weight extended X-ray absorption fine structure (EXAFS) spectra for Pt₁/FeO_x before and after calcination. Similar to our previous reports³, no Pt–Pt bond contribution was found. This observation is in marked contrast to the significant sintering typically noted for small metal species/atoms sintered to calcination at elevated temperature^{38,39}, and indicates a very strong interaction between Pt atoms and Fe₂O₃ that inhibits migration and sintering of the former. X-ray absorption near edge structure (XANES) measurements confirmed that the chemical state of Pt atoms before and after calcination resembled that PtO₂ with tetravalent Pt(IV) (Supplementary Figure 2d) rather than metallic platinum with zerovalent Pt(0)³.

Pt NP-generated high loading Pt SACs on Fe₂O₃ support. Pt NPs are known to liberate mobile PtO₂ species at elevated temperature under an oxidizing atmosphere⁴⁰, which may be subsequently trapped by either larger Pt NPs (Ostwald ripening) or unique oxide sites or crystalline facets resulting in metal dispersion^{41–45}. In the present case, wherein a strong interaction between Pt atoms and the Fe₂O₃ support is apparent, we anticipate that Pt atoms vaporized from a NP could be trapped and stabilized by the Fe₂O₃ surface. To test this hypothesis, pre-formed colloidal Pt NPs were supported on Fe₂O₃ at a 0.3 wt% loading and the ethylene glycol stabilizer was removed by a 500 °C calcination (denoted as 0.3Pt/Fe₂O₃-NP), prior to various high-temperature calcination treatments. HAADF-STEM imaging revealed the presence of 2–3 nm diameter Pt NPs (Supplementary Figure 3a–b). In contrast to Pt₁/FeO_x materials, CO DRIFTS of 0.3Pt/Fe₂O₃-NP exhibited both bridging (1839 cm⁻¹) and coverage dependent linear bound CO (2072–2064 cm⁻¹) (Supplementary Figure 3c), which is consistent with extended arrays of Pt atoms. Higher temperature calcination (800 °C, 5 h) resulted in the complete disappearance of these Pt NPs (denoted as 0.3Pt/Fe₂O₃-C800, Supplementary Figure 4a), and concomitant formation of a very high density of isolated Pt atoms (Supplementary Figure 4b). Fig. 2 presents the Fourier transform radial distribution function of the Pt L_{III}-edge *k*³-weighted EXAFS spectrum of 0.3Pt/Fe₂O₃-C800, alongside reference distribution functions for Pt foil and PtO₂ (corresponding EXAFS spectra and fits appear in Supplementary Figure 5 and Supplementary Table 1). Two prominent scattering distances are observed for 0.3Pt/Fe₂O₃-C800 at ~1.7 Å and 2.7 Å attributed to Pt–O and Pt–Fe contributions^{3,27}, respectively, confirming only the sole presence of atomically-dispersed Pt atomic species.

Note that some Pt NPs remained visible by electron microscopy after a lower temperature (600 °C) calcination, albeit more loosely coordinated to the underlying support (Supplementary Figure 4c). An oxidizing atmosphere was critical to observe this high-temperature dispersion; annealing 0.3Pt/Fe₂O₃-NP under Ar at 800 °C promoted Pt aggregation into larger 3–5 nm particles (Supplementary Figure 4d). This observation strongly implicates oxidized Pt species in Pt NP dispersion (Fig. 3), and indeed X-ray photoelectron spectra (XPS) (Supplementary Figure 6c) provide direct evidence for high-valent (near +IV) Pt in the 0.3Pt/Fe₂O₃-C800 catalyst. This is quite different from those divalent (+II) Pt ions dominating on CeO₂ support after high-temperature calcination^{46,47}, and hence further evidences a stronger Pt–Fe₂O₃ interaction that partially arises from covalent bonding interaction^{48,49}. Three requirements emerge for the successful conversion of Pt NPs into atomically dispersed Pt: a

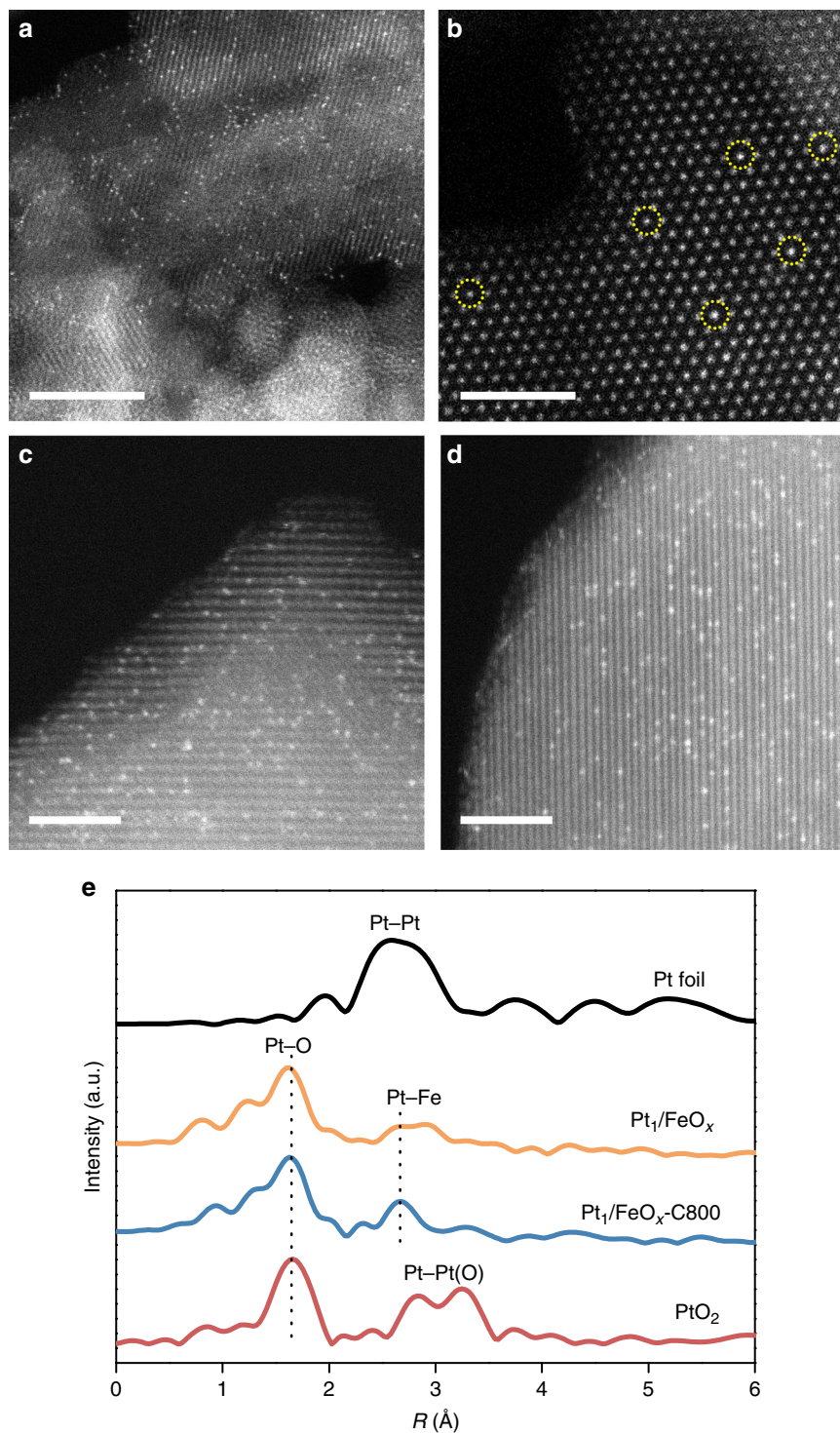


Fig. 1 Structure of Pt_1/FeO_x . **a, b** AC-HAADF-STEM images of Pt_1/FeO_x , and **c, d** Pt_1/FeO_x -C800, highlighting atomically dispersed Pt (circled in **b**). 5 nm scale bar for panel **a**, and 2 nm scale bars for **b, c, d**. **e** Fourier transform radial distribution function of the Pt L_{III} -edge k^3 -weighted EXAFS spectra of Pt_1/FeO_x before and after calcination in comparison with PtO_2 and Pt foil

high temperature to promote Pt mobility; the presence of molecular O_2 to partially oxidize the surface of Pt NPs, thereby enabling vaporization of (mobile) PtO_2 ; and a strong interaction between support and surface Pt atoms. Consequently, highly stable static single atoms on heterogeneous surface can be fabricated⁵⁰.

The first condition is met for H_2PtCl_6 functionalized $\alpha\text{-Al}_2\text{O}_3$ (Supplementary Figure 7a–b) subjected to the same high-temperature processing. However, in this case the weak metal-

support interaction favors Ostwald ripening and the growth of large (10–50 nm) Pt particles (Supplementary Figure 7c–d) over their dispersion, as previously reported⁴². Since the particle size in the fresh sample ranges from 2–20 nm (Supplementary Figure 7b), and the dynamics of Pt NP dispersion into Pt atoms are related to particle size⁵¹, a control experiment was further performed, in which 2–3 nm Pt NPs were deposited over Al_2O_3 (Supplementary Figure 7e–f). Sintering was again observed after heat treatment (Supplementary Figure 7g–h), confirming a weak interaction

between alumina and Pt species. We note that dispersion of < 1 nm Pt NPs was recently reported over MCM-22⁵¹, which may reflect restricted migration of Pt species through the microporous zeolite network.

Having identified conditions under which Pt NPs can be dispersed over an Fe_2O_3 surface, we explored the effect of Pt loading with a view to maximizing the density of isolated atoms achievable, and thereby compensate for the extremely low surface area (only $5\text{--}10\text{ m}^2\text{ g}^{-1}$) of the Fe_2O_3 support after the requisite 800°C calcination. A higher 1 wt% loading of the same $2\text{--}3$ nm Pt NPs (denoted as 1Pt/ Fe_2O_3 -NP) were also fully transformed into isolated atoms by calcination at 800°C (Supplementary Figure 8a–b). Low energy ion scattering (LEIS) evidenced a clear decrease in the Pt:Fe atomic ratio in the outermost surface layer upon calcining the stabilizer free 1Pt/ Fe_2O_3 -NP to 800°C (Supplementary Figure 9). Since the total Pt loading determined by inductively coupled plasma spectrometry-atomic emission spectrometry (ICP-AES) remained unchanged, it appears that

some Pt atoms diffuses into the near sub-surface region of the Fe_2O_3 support, possibly by a cation-exchange process^{52,53}. However, a further increase in Pt loading to 2 wt% resulted in the formation of Pt clusters alongside isolated atoms (Supplementary Figure 8c–d), in line with the theoretical maximum loading (~ 1.5 wt% for Fe_2O_3 possessing a surface area of $10\text{ m}^2\text{ g}^{-1}$, see Methods). A high density of clusters and few single isolated atoms were observed for a 4.5 wt% Pt loading (Supplementary Figure 8e–f). The maximum concentration of atomically-dispersed Pt loading is clearly dictated by the very low support surface area. The emergence of Pt clusters for loadings ≥ 2 wt% confirms that any Pt atoms diffusing into the support must be confined to the immediate subsurface region and not migrated into the bulk Fe_2O_3 lattice, since the latter pathway would enable isolated atoms to remain the dominant surface species at far higher Pt loadings.

Disintegration of Pt NPs during high-temperature calcination was directly visualized by in situ HAADF-STEM, and one Fe_2O_3 crystal of 1Pt/ Fe_2O_3 -NP sample was randomly picked to observe the process. Prior to calcination, about 300 Pt particles were visible across the Fe_2O_3 support, and the average particle size was about 3 nm (Fig. 4a–c). However, after heating to 800°C under a flow of 1 bar O_2 for 20 min, the total number of Pt NPs decreased to ~ 200 , since many of the $2\text{--}3$ nm Pt NPs shrank and/or disappear entirely, while a few larger particles (size above 10 nm) remained (Fig. 4b–c versus Fig. 4e–f). The loss of small clusters was confirmed by higher resolution, time-resolved imaging (Fig. 4g–i taken from the Supplementary Movie 1), which reveal smaller Pt clusters (e.g., particle 1) disintegrated in less than 35 s, while larger Pt clusters (e.g., particle 2) vanished in 45 s. Previous reports suggest that smaller metal crystallites disperse as adatoms, which migrate towards neighboring (larger) particles and eventually coalesce at elevated temperature via Ostwald Ripening, driven by lowering of the total surface energy⁵⁴. In this case, however, particle disappearance occurs in the absence of such coalescence, consistent with the accompanying genesis of atomically-dispersed Pt entities.

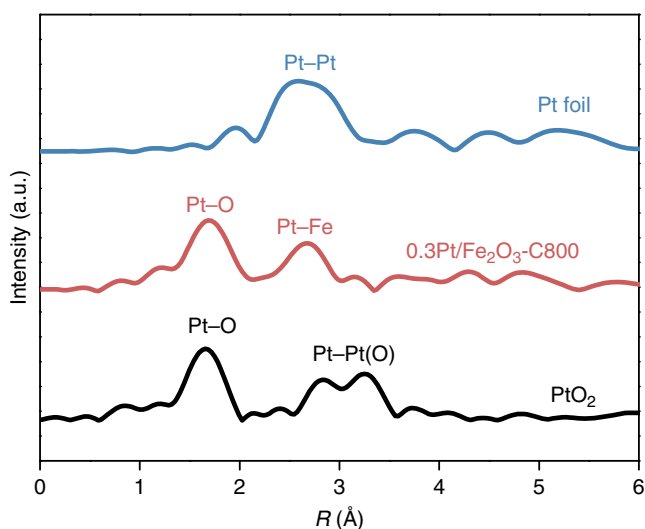


Fig. 2 X-ray absorption spectroscopy of the 0.3Pt/ Fe_2O_3 -C800 catalyst. Fourier transform Pt L_{III} -edge radial distribution functions of the 0.3Pt/ Fe_2O_3 -C800 catalyst in comparison with PtO_2 and Pt foil

DFT Studies. The preceding electron microscopy, X-ray spectroscopy and diffraction, and CO chemisorption measurements provide both clear evidence of, and insight into the driving force for, the formation of atomically-dispersed Pt following high-

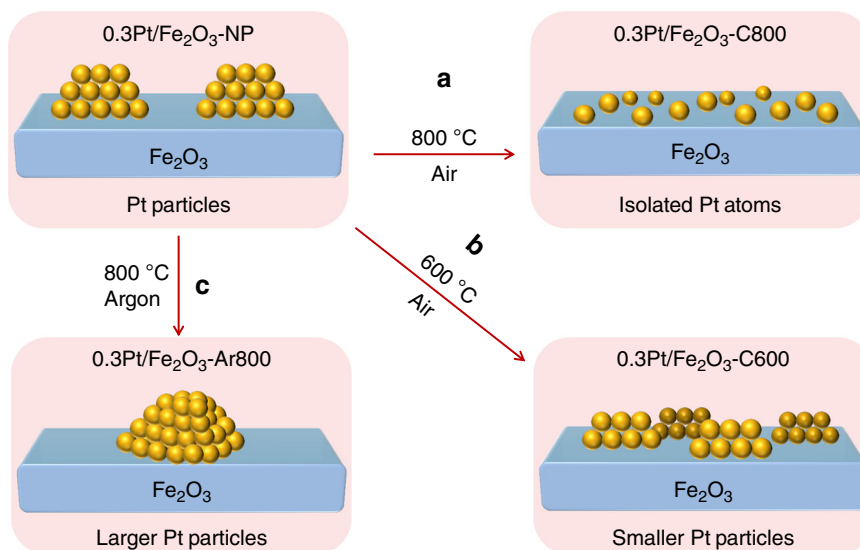


Fig. 3 Illustration of thermally induced Pt nanoparticle restructuring. **a, b** Calcination under oxygen, or under an inert atmosphere (**c**), resulting in dispersion as single-atoms or particle sintering, respectively

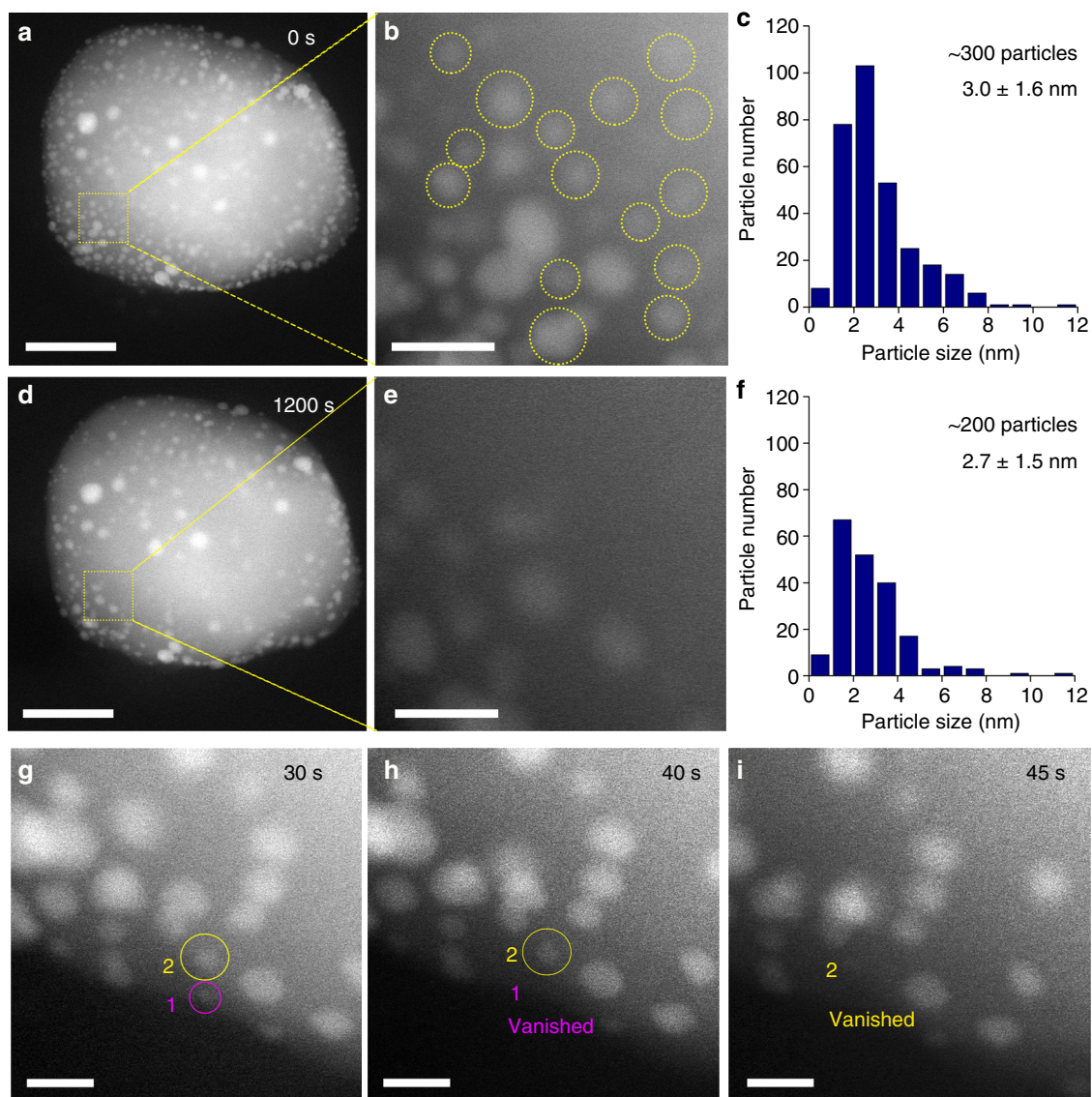


Fig. 4 In situ characterization of Pt NP oxidative dispersion. **a–c** HAADF-STEM images and size distribution histogram of 1Pt/Fe₂O₃-NP before, and **d–f** after in situ calcination at 800 °C under 1 bar flowing O₂ for 20 min: the yellow squares in panels a and d show the same sample area. A 50 nm scale bars in **a, d** and 10 nm scale bars in **b, e**. Yellow circles in panel b highlighted the particles missing after calcination for 20 min. **g–i** Sequential HAADF-STEM images from the same area showing the dissociation of small particles (labeled by purple and yellow circles) during in situ calcination: 5 nm scale bars; elapsed time (in seconds) indicated in upper right corner of each image

temperature calcination; NP dispersion is triggered by the formation of PtO₂ (Supplementary Figure 6). Computational modeling via DFT calculations (Fig. 5a–b) suggests that the evaporation free energy of PtO₂ (the dominant surface species under an oxidizing environment) from a Pt(221) step (model in Supplementary Figure 10) is about -0.61 eV per PtO₂ at 800 °C, whereas the evaporation energy of Pt₁ (the dominant species under inert environments, Supplementary Figure 4d) can reach as high as 4.00 eV, and hence is energetically strongly disfavoured due to CMSI of Pt₁ to the surface atoms. By comparison, PtO₂ evaporation at 600 °C is virtually thermo-neutral or slightly endothermic (0.07 eV), indicating the critical role of temperature in dispersing Pt NPs. This result is consistent well with the experimental results that the dispersion of NPs only occurred with calcination >600 °C (Fig. 3, Supplementary Figures 4a–c).

This temperature-dependent evolution of PtO₂ dissociation energetics from a Pt(221) step (representative of the partially oxidized surface of Pt NPs following high-temperature

calcination) mirrors that of the catalytic activity for methane oxidation, as discussed below. The dissociative adsorption of PtO₂ on an oxygen terminated Fe₂O₃(0001) surface (and concomitant desorption of one O₂ molecule) is highly exothermic at 800 °C (calculated as -2.46 eV, Fig. 5c–d), with PtO₂ dissociative capture even more favorable at lower temperature. Note that the evaporation, migration, and trapping do not require the presence of anion or cation vacancies on the support: no Lewis acid sites were detected on the Fe₂O₃ support by NH₃ temperature-programmed desorption, suggesting that Fe₂O₃ possessed negligible oxygen anion defects following a high-temperature calcination. Therefore, Pt atoms disperse across the ferric oxide support where they are anchored as isolated atoms through a strong local surface interaction. Calculations indicate that these reactively-formed Pt atoms coordinate with four surface oxygen atoms in a distorted square geometry with an average Pt–O length of 1.94 Å, intermediate between that in gas PtO₂ (CN = 2, 1.70 Å) and bulk PtO₂ (CN = 6, 2.04 Å). Bader charge analysis of an isolated Pt

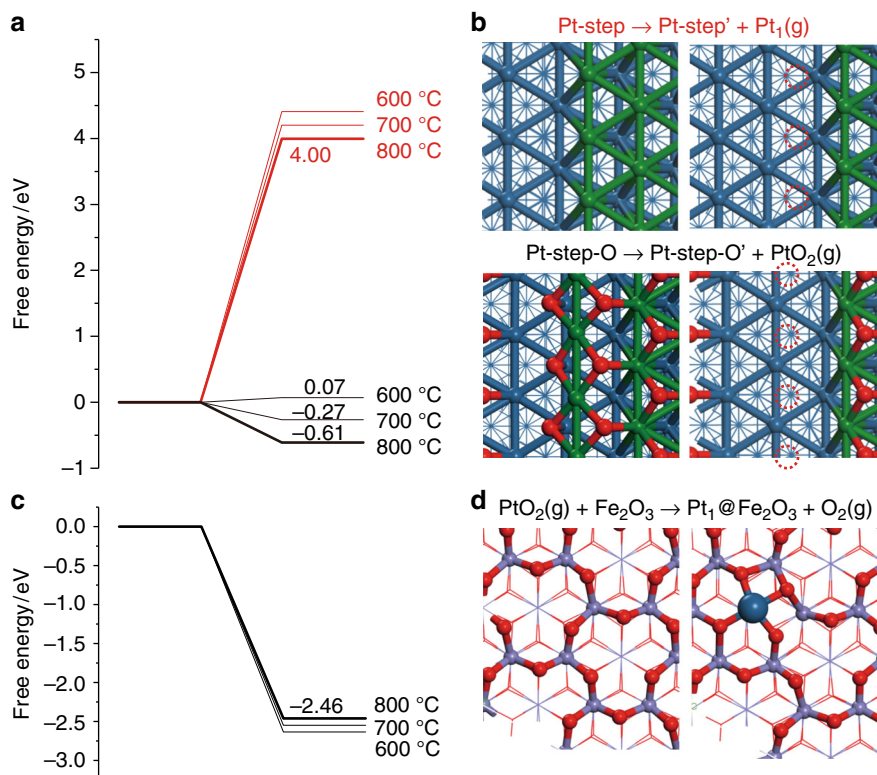


Fig. 5 Optimized structures and energy profiles for Pt NP dispersion as isolated Pt atoms. **a, b** Calculated energies and surface structures for evaporation of a single Pt atom (Pt₁) from a Pt(221) step (red value) or evaporation of a PtO₂ species from an oxygen pre-covered Pt(221) step (black values). **c, d** Calculated energies and surface structures for dissociative capture of PtO₂ over Fe₂O₃(0001) surface and concomitant formation of a Pt₁ atom and evolved O₂. Color code: outermost layer Pt (green); second layer Pt (blue); O (red); Fe (purple)

atom on Fe₂O₃(0001) shows a charge of + 1.43 |e|, approximating to but slightly lower than the charge of Pt in gas PtO₂ and bulk PtO₂ (Supplementary Table 2), consistent with tetravalent Pt and the XPS analysis (Supplementary Figure 6). The total free energy change for the formation of Fe₂O₃ stabilized isolated Pt atoms from Pt NPs is -3.07 eV per Pt atom at 800 °C, i.e. such a dispersion is strongly exothermic with low barrier. In comparison, Pt only interacts very weakly (low endothermic free energy) with an alumina surface (Supplementary Figures 11–13, Supplementary Table 3). By comparing the charge density difference of Pt₁/Fe₂O₃(0001) and Pt₁/Al₂O₃(010), defined as $\Delta\rho = \rho_{\text{Pt+slab}} - \rho_{\text{slab}} - \rho_{\text{Pt}}$, four strong chemical bonds are observed between Pt and adjacent O atoms by covalent (*d-p*) orbital interactions at the Fe₂O₃ surface. In contrast, only very weak Pt–O interactions occur at the Al₂O₃ surface, resulting in Pt–O bond lengths much longer than that on Fe₂O₃. Bader analysis indicates that each Pt possesses a -0.14 |e| charge, i.e. approximately metallic character (Supplementary Table 2); both findings are attributed to the irreducibility of Al³⁺, i.e. strong non-redox Al–O bonding network, which prevents any significant metal-support interaction. DFT calculations are hence in excellent agreement with experimental observations. The finding of the stability of SAC closely related to the reducibility of the support is consistent with previous work as well⁵⁵.

Catalytic performance in methane combustion. The impact of oxygen-induced restructuring at elevated temperature on catalytic performance is striking (Fig. 6). As the reaction temperature of 1Pt/Fe₂O₃-NP under an oxygen-rich methane gas feed was raised from 300 to 700 °C, the combustion activity increased such that a modest ~18 % conversion was initially attained. However, in contrast to most catalytic reactions wherein activity subsequently

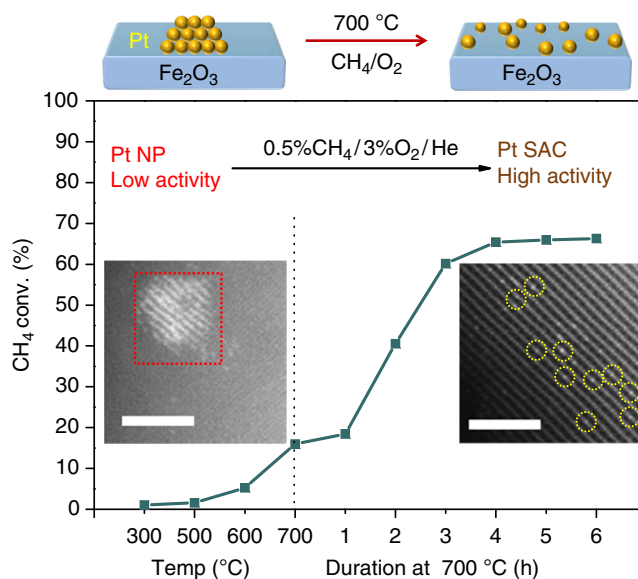


Fig. 6 Dynamic formation of a Pt SAC during methane oxidation. Light-off curve of 1Pt/Fe₂O₃-NP for methane oxidation with a feed gas comprising 0.5 vol% CH₄/ 3 vol% O₂/ 97 vol% He balance at 30 mLmin⁻¹. STEM images of catalyst before (left-inset) and after (right-inset) reaction. Scale bars, 2 nm. Red square and yellow circles are used to indicate the Pt NP and Pt atoms, respectively

decreases with time-on-stream, the activity of 1Pt/Fe₂O₃-NP displayed a monotonic increase over the following 4 h at 700 °C to reach 65 % conversion. Post-reaction catalyst characterization confirmed that this high-temperature catalyst activation was

accompanied by the disappearance of Pt NPs present in the as-prepared material (Fig. 6 left inset), and formation of atomically-dispersed Pt (Fig. 6 right inset, Supplementary Figure 14a–b), demonstrating a causal relationship between in situ genesis of a Pt SAC and dramatically enhanced performance. Note that pre-activation of 1Pt/Fe₂O₃-NP by calcination at 700 °C for 5 h prior to methane addition resulted in an extremely stable Pt SAC that maintained similar activity for > 16 h on-stream (Supplementary Figure 14c). Since the mass of 1Pt/Fe₂O₃-NP catalyst (and Pt loading) in this methane light-off experiment is constant, the time-dependent increase in CH₄ conversion at 700 °C due to catalyst restructuring is directly proportional to the catalytic activity; single-atom formation induces a four-fold enhancement (18→65 % conversion) in the specific activity. Additional experiments with the same catalyst at 20 % iso-conversion in either its SAC (1Pt/Fe₂O₃-C700) or nanoparticulate (1Pt/Fe₂O₃-NP) form confirmed that the specific activity of the former was 4 times greater than that of the latter (2.01 mol_{CH₄} h⁻¹ g_{Pt}⁻¹ vs. 0.47 mol_{CH₄} h⁻¹ g_{Pt}⁻¹) and 20 times than that reported for Pt/Al₂O₃⁵⁶ (Supplementary Table 4). Turnover frequencies based on the number of surface Pt atoms (dispersion) were similar for SAC and nanoparticulate counterparts (0.1 s⁻¹ vs. 0.08 s⁻¹), indicating a common active site, and hence the superior specific activity of the single-atom catalyst reflects its improved atom efficiency (every Pt atom directly activates methane).

Interaction between Pt atoms and iron-modified support.

Fundamental insight into the reaction-induced restructuring of metal NPs over a reducible metal oxide support offers a facile route to synthesize high-loading and thermally stable SACs. Platinum NPs introduced either as pre-formed colloids or e.g. by simple wet impregnation with 1 wt% H₂PtCl₆ (Supplementary Figure 15a–b) over a low area Fe₂O₃ support, are readily transformed into isolated Pt atoms by high-temperature calcination (Supplementary Figure 15c–d). Flytzani-Stephanopoulos and co-workers have shown that Na or K ions can stabilize surface hydroxyls, which can in turn stabilize metal (Au and Pt) atoms and/or subnanometer clusters over diverse supports^{57–59}. However, our recent work⁶⁰ has not identified such a role for alkalis, suggesting that Fe₂O₃ may have unique properties to some degree. To test our hypothesis, we synthesized a sodium-free material using a (NH₄)₂CO₃ precipitant, denoted as Fe₂O₃(N). Pt NPs exhibited the same dispersion and single-atom formation after 800 °C calcination over this Fe₂O₃(N) support (Supplementary Figure 16), confirming that the reducible Fe₂O₃ support, and not presence of Na⁺, was responsible for stabilizing Pt single-atoms.

The propensity for stabilizing single Pt atoms is dictated by the magnitude of the metal-support interaction, which itself can be tuned by e.g. doping a reducible (Fe₂O₃) into a non-reducible (Al₂O₃) oxide (Supplementary Figure 17a) through co-precipitation. As shown in Fig. 7, functionalization of such an Fe₂O₃-Al₂O₃ mixed metal oxide by Pt NPs, and subsequent 800 °C calcination, delivers atomically-dispersed Pt precisely as observed over the pure ferric oxide (Supplementary Figure 17b–c), but in a higher area form (~30 m² g⁻¹).

Discussion

We reported a facile synthesis of thermally-stable Pt SAC that achieved remarkable catalytic performance towards methane combustion. Isolated Pt atoms with high oxidation state are not stabilized by surface defects but through a strong covalent interaction with iron and oxygen atoms on the surface. Since Fe can be simply incorporated into a variety of oxides with low area and/or defect density, e.g. perovskites and spinels, our approach

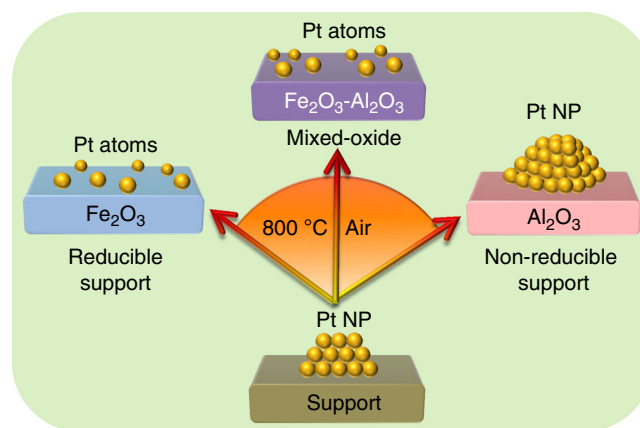


Fig. 7 Illustration of Pt NP sintering/dispersing on different supports. Metal oxide reducibility dictates the ability of a support to anchor isolated Pt atoms: Fe₂O₃ favors atomically dispersed Pt, whereas Al₂O₃ favors nanoparticle sintering. Doping iron oxide into non-reducible support (Fe₂O₃-Al₂O₃) can adjust noble metal dispersion

may afford a generic route to fabricate high loading Pt SACs over diverse supports being able to operate under harsh reaction conditions.

Methods

Synthesis of FeO_x and Fe₂O₃. Ferric nitrate (Fe(NO₃)₃·9H₂O, 98%, Sigma-Aldrich) and sodium carbonate (Na₂CO₃, 99.5% Sigma-Aldrich) were used as purchased. An aqueous solution of Fe(NO₃)₃ (1 mol L⁻¹) was obtained by dissolving Fe(NO₃)₃·9H₂O (122 g, 0.3 mol) in deionized water (300 mL). FeO_x was subsequently prepared from this solution by precipitation. First, Na₂CO₃ (11 g) was added in water (100 mL) and stabilized at 50 °C in a water bath. To this, 40 mL Fe(NO₃)₃ solution was slowly added (1 mL min⁻¹) under vigorous stirring at 50 °C for 3 h, and then aged static for a further 2 h. The recovered FeO_x solid was washed with deionized water and dried at 60 °C overnight. Fe₂O₃ was obtained by calcining FeO_x at 800 °C (ramp rate 3 °C min⁻¹) for 5 h under flowing air (100 mL min⁻¹).

Synthesis of Fe₂O₃(N). Ferric nitrate (Fe(NO₃)₃·9H₂O, 98%, Sigma-Aldrich) and ammonium carbonate (Sigma-Aldrich, (NH₄)₂CO₃ 99.5%) were used as purchased. First, (NH₄)₂CO₃ (4 g) was added in water (6 mL) and stabilized at 50 °C in a water bath. To this, 20 mL Fe(NO₃)₃ solution (1 mol L⁻¹) was slowly added (1 mL min⁻¹) under vigorous stirring at 50 °C for 3 h, and then aged static for a further 2 h. The recovered FeO_x solid was washed with deionized water and dried at 60 °C overnight. Fe₂O₃(N) was obtained by calcining FeO_x at 800 °C (ramp rate 3 °C min⁻¹) for 5 h under flowing air (100 mL min⁻¹) to obtain the Na⁺-free support.

Synthesis of Fe₂O₃-Al₂O₃. An Fe₂O₃-Al₂O₃ mixed oxide was synthesized by co-precipitation. Fe(NO₃)₃·9H₂O (8 g, 0.02 mol) and Al(NO₃)₃·9H₂O (7.5 g, 0.02 mol, 98%, Sigma-Aldrich) were first dissolved in 80 mL deionized water. Separately, (NH₄)₂CO₃ (7.7 g, 0.08 mol, 99%, Sigma-Aldrich) was dissolved in 80 mL deionized water. The two aqueous solutions were combined in 30 mL water at 50 °C under stirring for 3 h, and then aged static for a further 2 h. The resulting solid was recovered by filtration, washed with deionized water, dried at 60 °C overnight, and finally calcined at 800 °C (ramp rate 3 °C min⁻¹) for 5 h under flowing air (100 mL min⁻¹).

Synthesis of Pt₁/FeO_x and Pt₁/FeO_x-C800. Pt₁/FeO_x was prepared by co-precipitation of an aqueous mixture of chloroplatinic acid (H₂PtCl₆·6H₂O, 37 mg Pt mL⁻¹, 2.6 mL, 99.9%, Sigma-Aldrich) and Fe(NO₃)₃·9H₂O (1 mol L⁻¹, 40 mL) with Na₂CO₃ solution (11 g Na₂CO₃ in 100 mL H₂O) at 50 °C under stirring for 3 h, and ageing static for a further 2 h. The resulting solid was recovered by filtration, washed with deionized water and dried at 60 °C overnight. A portion of the Pt₁/FeO_x was then calcined as above at 800 °C and denoted as Pt₁/FeO_x-C800. The Pt loading determined by ICP was 1.8 wt%.

Synthesis of xPt/Fe₂O₃-NP and xPt/Fe₂O₃-C800. Pt nanoparticles (NPs) were synthesized according to the literature⁶¹. Typically, an ethylene glycol solution of NaOH (0.5 mol L⁻¹) was added into an ethylene glycol solution of H₂PtCl₆·6H₂O under stirring (3.7 mg Pt mL⁻¹). The resulting transparent yellow platinum colloidal solution was heated at 160 °C for 3 h under flowing Ar to form a transparent dark-brown platinum colloidal solution. Separately, Fe₂O₃ was dispersed in deionized water by sonication, to which the Pt NP colloidal solution was added, and the

resulting solid dried overnight at 100 °C, and then calcined at 500 °C for 5 h under flowing air to remove the glycol stabilizer. A series of Pt NP catalysts were prepared with different Pt loadings, denoted as xPt/Fe₂O₃-NP ($x = 0.3, 1, 2, \text{ or } 4.5 \text{ wt\% Pt}$ as determined by ICP). xPt/Fe₂O₃-C800 was obtained by treating xPt/Fe₂O₃-NP under flowing air (100 mL min⁻¹) at 800 °C for 5 h.

Synthesis of Pt/Al₂O₃-NP and Pt/Al₂O₃-C800. Pt/Al₂O₃-NP was prepared following the above procedure by dispersing colloidal Pt over the Al₂O₃ support at a Pt loading of 0.3 wt% as determined by ICP, and then calcined at 300 °C for 5 h under flowing air. Pt/Al₂O₃-C800 was obtained by treating Pt/Al₂O₃-NP under flowing air (100 mL min⁻¹) at 800 °C for 5 h.

Synthesis of Pt/Fe₂O₃-Al₂O₃-NP and Pt/Fe₂O₃-Al₂O₃-C800. Pt/Fe₂O₃-Al₂O₃-NP and Pt/Fe₂O₃-Al₂O₃-C800 were prepared following the above procedure by dispersing colloidal Pt over the Fe₂O₃-Al₂O₃ support at a Pt loading of 0.5 wt% as determined by ICP.

Synthesis of 0.3Pt/Fe₂O₃-C600 and 0.3Pt/Fe₂O₃-Ar800. 0.3Pt/Fe₂O₃-C600 was obtained by treating 0.3Pt/Fe₂O₃-NP under flowing air (100 mL min⁻¹) at 600 °C for 5 h. 0.3Pt/Fe₂O₃-Ar800 was obtained by treating 0.3Pt/Fe₂O₃-NP under flowing Ar (100 mL min⁻¹) at 800 °C for 5 h.

Synthesis of H₂PtCl₆/Fe₂O₃ and H₂PtCl₆/Fe₂O₃-C800. In a typical procedure, 1 g Fe₂O₃ was dispersed in 5 mL deionized water by sonication, to which 0.3 mL H₂PtCl₆ aqueous solution (37 mg_{Pt} mL⁻¹) was added. Water was gradually evaporated by heating the resulting suspension at 80 °C. The resulting solid was calcined at 300 °C for 5 h under flowing air (100 mL min⁻¹) and denoted as H₂PtCl₆/Fe₂O₃. The Pt loading was 1 wt% as determined by ICP. A portion of H₂PtCl₆/Fe₂O₃ was also heated at 800 °C under flowing air (100 mL min⁻¹) for 5 h to generate H₂PtCl₆/Fe₂O₃-C800.

Synthesis of H₂PtCl₆/Fe₂O₃(N) and H₂PtCl₆/Fe₂O₃(N)-C800. In a typical procedure, 150 mg Fe₂O₃(N) was dispersed in 2 mL deionized water by sonication, to which 0.013 mL H₂PtCl₆ aqueous solution (37 mg_{Pt} mL⁻¹) was added. Water was gradually evaporated by heating the resulting suspension at 80 °C. The resulting solid was calcined at 300 °C for 5 h under flowing air (100 mL min⁻¹) and denoted as H₂PtCl₆/Fe₂O₃(N). The Pt loading was 0.2 wt% as determined by ICP. A portion of H₂PtCl₆/Fe₂O₃ was also heated at 800 °C under flowing air (100 mL min⁻¹) for 5 h to generate H₂PtCl₆/Fe₂O₃(N)-C800.

Synthesis of H₂PtCl₆/Al₂O₃ and H₂PtCl₆/Al₂O₃-C800. α -Al₂O₃ (99.5%, Sigma-Aldrich) was used as purchased. H₂PtCl₆/Al₂O₃ and H₂PtCl₆/Al₂O₃-C800 were prepared following the above procedure by dispersing H₂PtCl₆ over the α -Al₂O₃ support. The Pt loading was 1 wt% as determined by ICP.

Characterization. Pt loadings were determined by inductively coupled plasma spectrometry-atomic emission spectrometry (ICP-AES) on an IRIS Intrepid II XSP instrument (Thermo Electron Corporation). X-ray diffraction (XRD) patterns were collected on a PW3040/60 X'Pert Pro super (PANalytical) diffractometer, operating at 40 kV and 40 mA using a Cu K α radiation source ($\lambda = 0.15432 \text{ nm}$) with a scanning angle (2θ) of 10–80°. In situ diffuse reflectance infrared Fourier transform spectra (DRIFTS) were collected at 25 °C with a Bruker Vertex 70 spectrometer equipped with a mercury cadmium telluride (MCT) detector at a resolution of 4 cm⁻¹ over 32 scans. Samples were first heated in situ at 200 °C under flowing He for 0.5 h, then cooled to room temperature prior to recording of background spectra. Subsequently, a 1 vol% CO/He flow was introduced to the sample for 10 min. The environmental cell was then purged with flowing helium to remove gas phase CO, prior to spectral acquisition of chemisorbed CO species. Temperature-programmed desorption (TPD) was conducted on a Micromeritics AutoChem II 2910 automatic catalyst characterization system equipped with a mass spectrometer. First, the Fe₂O₃ support was loaded into a U-shape quartz reactor and pretreated at 200 °C in He for 0.5 h to remove adsorbed hydrates and carbonates. After cooling to 60 °C, NH₃ gas pulses were injected until a stable signal was obtained, and the sample then heated to 900 °C under He at 10 °C min⁻¹. Synchrotron radiation experiments were performed at BL14B2 of SPring-8⁶² and BL14W1 of the SSRF light sources. Pt L_{III}-edge transmission X-ray absorption spectra were acquired on samples loaded into the Al₂O₃ tube, in addition to Pt foil and PtO₂ powder references. Spectra were background subtracted, normalized, and fitted using the IFEFFIT software suite⁶³. X-ray photoelectron spectra (XPS) were performed on a VG ESCALAB MK2 apparatus using Al K α radiation (1486.6 eV, 12.5 kV, 250 W) to obtain the binding energies and oxidation states of Pt. Binding energies are referenced to adventitious carbon at 284.8 eV. High-angle annular dark-field scanning transmission electron microscopy (HAADF-STEM) images were obtained on a JEOL JEM-2100F. Aberration-corrected HAADF-STEM images were obtained on a JEOL JEM-ARM200F equipped with a CEOS probe corrector. Samples were dispersed by ultrasonication in ethanol, and the resulting solution

dropped on to carbon films supported on copper grids. In situ imaging was performed on a Titan Cubed Themis G2 300 microscope using a DENSsolutions Climate S3 and Gas flow and Heating System, which comprised a heated sample holder and gas delivery manifold. The sample was mounted in a 5 μm gap between two 30 nm thick SiN windows. The oxygen purity used for the in situ calcination experiment was 99.999%. Reported temperatures were based on the DENSsolutions calibration. Low energy ion scattering (LEIS) spectra were acquired on a Kratos AXIS Supra spectrometer using 1 keV He⁺ ions generated from a Minibeam 6 Gas Cluster Ion Source, at a scattering angle of 130 °, and 320 eV analyzer pass energy, averaged over a sample area of 500 μm^2 .

Catalytic evaluation. CH₄ oxidation was performed in a U-shaped quartz reactor using 20 mg catalyst and a feed gas comprising 0.5 vol% CH₄, 3 vol% O₂, and 97 vol% He balance at 30 mL min⁻¹. The effluent gas composition was analyzed by an on-line Agilent 6890 A gas chromatograph equipped with a TDX-01 column and a thermal conductivity detector. CH₄ conversion was calculated based on the difference between inlet and outlet concentrations.

Turnover frequency (TOF) calculation. TOFs were calculated from specific activities measured at 700 °C and approximately 20 % CH₄ iso-conversion for 17 mg 1Pt/Fe₂O₃-NP and 6 mg 1Pt/Fe₂O₃-C700 catalysts respectively. A common gas flow rate of 50 mL min⁻¹ was used, resulting in a space velocity of 176,000 mL h⁻¹ g_{cat}⁻¹ for 1Pt/Fe₂O₃-NP and 500,000 mL h⁻¹ g_{cat}⁻¹ for 1Pt/Fe₂O₃-C700. The Pt dispersion of 1Pt/Fe₂O₃-NP was calculated according to the following relationship between the dispersion (D) and particle radius (r): $D / \% = 100 \times 5.6 / r_{\text{Pt}}$. The average particle radius of 1Pt/Fe₂O₃-NP was 15 Å (Fig. 4c), corresponding to a dispersion of 30 %, while that for 1Pt/Fe₂O₃-C700 was 100 %. TOFs were calculated by normalizing specific activities to the product of the dispersion and total Pt_{mols} (identical for both catalysts).

DFT parameters. All DFT + U calculations were performed using spin-polarized density functional theory (DFT) with the generalized gradient approximation (GGA) and Perdew-Burke-Ernzerhof (PBE) exchange-correlation functional as implemented in VASP5.3.5^{64–66}. The U-J value of 3.0 eV was used to describe the strong correlation of the localized Fe 3d states^{3,67,68}. Valence states of all atoms were expanded in a plane wave basis set with a cutoff energy of 400 eV, and a Monkhorst-Pack mesh of 3 × 3 × 1 k points was used for Brillouin Zone integration. Atomic positions were optimized by the conjugate gradient algorithm until forces were < 0.02 eV/Å. Free energy changes were calculated from zero-point energies, enthalpies, and entropies of gas Pt single atom and PtO₂ species corrected at 600, 700 and 800 °C, respectively as summarized in Supplementary Table 3.

Computational models. A Pt(221)-p(3 × 1) surface slab was used to model the step and edge of Pt NPs (coordination number = 7 for atoms at edges). We applied periodic models of surface slabs with five atomic layers, with the bottom two layers frozen and the remaining layers allowed to relax. The (0001) surfaces of α -Fe₂O₃-p(2 × 2) were also represented by a periodic slab model. Antiferromagnetic properties of α -Fe₂O₃ were represented by a (+ - - +) magnetic configuration, which was previously proven to be most energetically favorable for α -Fe₂O₃³. We chose slabs containing 9 layers of Fe atoms and 5 atomic layers of O to model the O-terminated surface. The bottommost Fe-O layers were frozen during geometry optimization. A θ -Al₂O₃(010)-p(4 × 2) surface slab was used to model the alumina substrate, consisting of six O-Al layers, wherein the bottom two O-Al layers were frozen while the remaining layers were allowed to relax^{69,70}. The IDIPOL tag was set to 3 to switch on dipole corrections to the total energy along the z-direction. All supercell slabs were periodically repeated with a 15 Å vacuum layer between surfaces in the direction of the surface normal.

Theoretical maximum loading of dispersed Pt atoms over Fe₂O₃ support. The BET surface area of Fe₂O₃ was 5–10 m² g⁻¹, hence 1 g of Fe₂O₃ provides ~5–10 m² of surface (S). Our DFT calculation model indicates that the maximum density of atomically dispersed Pt (D) is 4.5 atom nm⁻². The total number of isolated Pt atoms (N) that could be achieved for 1 g of Pt/Fe₂O₃ is therefore predicted to be $N = D \times S$. Since the mass of Pt (m) equals $N/N_A \times M$, where N_A is Avogadro's constant ($6.02 \times 10^{23} \text{ mol}^{-1}$), and M is the molar mass of Pt (195 g mol⁻¹), the theoretical maximum loading of isolated Pt atoms that could be dispersed over 1 g of Fe₂O₃ is $m(\text{g})/1(\text{g}) \times 100 \% = (D \times S / N_A) \times M \times 100 \% = 1.5 \text{ wt\%}$.

Data availability

The data that support the plots within this paper and other findings of this study are available from the corresponding authors upon reasonable request.

Received: 2 August 2018 Accepted: 6 December 2018

Published online: 16 January 2019

References

- Ertl, G., Knözinger, H., Schüth, F. & Weitkamp, J. *Handbook of Heterogeneous Catalysis*. 2nd edn, Vol. 1 (Wiley-VCH Verlag GmbH & Co. KGaA, Weinheim, 2008).
- Liu, L. & Corma, A. Metal catalysts for heterogeneous catalysis: from single atoms to nanoclusters and nanoparticles. *Chem. Rev.* **118**, 4981–5079 (2018).
- Qiao, B. et al. Single-atom catalysis of CO oxidation using Pt₁/FeO_x. *Nat. Chem.* **3**, 634–641 (2011).
- Yang, X.-F. et al. Single-atom catalysts: a new frontier in heterogeneous catalysis. *Acc. Chem. Res.* **46**, 1740–1748 (2013).
- Flytzani-Stephanopoulos, M. & Gates, B. C. Atomically dispersed supported metal catalysts. *Annu. Rev. Chem. Biomol. Eng.* **3**, 545–574 (2012).
- Mooiman, M. B., Sole, K. C., Dinham, N. *Metal Sustainability* (Wiley, Chichester, West Sussex, 2016).
- Zhang, X. et al. C-C Coupling on single-atom-based heterogeneous catalyst. *J. Am. Chem. Soc.* **140**, 954–962 (2018).
- Zhao, P. et al. Entrapped single tungstate site in zeolite for cooperative catalysis of olefin metathesis with Bronsted acid site. *J. Am. Chem. Soc.* **140**, 6661–6667 (2018).
- Bruix, A. et al. Maximum noble-metal efficiency in catalytic materials: atomically dispersed surface platinum. *Angew. Chem. Int. Ed.* **53**, 10525–10530 (2014).
- Fei, H. et al. General synthesis and definitive structural identification of MN₄C₄ single-atom catalysts with tunable electrocatalytic activities. *Nat. Catal.* **1**, 63–72 (2018).
- Malta, G. et al. Identification of single-site gold catalysis in acetylene hydrochlorination. *Science* **355**, 1399–1403 (2017).
- Gao, J. et al. Tuning chemical bonding of MnO₂ through transition-metal doping for enhanced CO oxidation. *J. Catal.* **341**, 82–90 (2016).
- Liu, G. et al. MoS₂ monolayer catalyst doped with isolated Co atoms for the hydrodeoxygenation reaction. *Nat. Chem.* **9**, 810–816 (2017).
- Li, T. et al. Maximizing the number of interfacial sites in single-atom catalysts for the highly selective, solvent-free oxidation of primary alcohols. *Angew. Chem. Int. Ed.* **57**, 7795–7799 (2018).
- Li, H. et al. Synergetic interaction between neighbouring platinum monomers in CO₂ hydrogenation. *Nat. Nanotechnol.* **13**, 411–417 (2018).
- Novotny, Z. et al. Ordered array of single adatoms with remarkable thermal stability: Au/Fe₃O₄(001). *Phys. Rev. Lett.* **108**, 216103 (2012).
- Upham, D. C. et al. Catalytic molten metals for the direct conversion of methane to hydrogen and separable carbon. *Science* **358**, 917–921 (2017).
- Marcinkowski, M. D. et al. Pt/Cu single-atom alloys as coke-resistant catalysts for efficient C-H activation. *Nat. Chem.* **10**, 325–332 (2018).
- Liu, P. et al. Photochemical route for synthesizing atomically dispersed palladium catalysts. *Science* **352**, 797–800 (2016).
- Chen, Z. et al. A heterogeneous single-atom palladium catalyst surpassing homogeneous systems for Suzuki coupling. *Nat. Nanotechnol.* **13**, 702–707 (2018).
- Shan, J., Li, M., Allard, L. F., Lee, S. & Flytzani-Stephanopoulos, M. Mild oxidation of methane to methanol or acetic acid on supported isolated rhodium catalysts. *Nature* **551**, 605–608 (2017).
- Cui, X. et al. Synthesis of single atom based heterogeneous platinum catalysts: high selectivity and activity for hydrosilylation reactions. *ACS Cent. Sci.* **3**, 580–585 (2017).
- Yang, B., Burch, R., Hardacre, C., Headdock, G. & Hu, P. Origin of the increase of activity and selectivity of nickel doped by Au, Ag, and Cu for acetylene hydrogenation. *ACS Catal.* **2**, 1027–1032 (2012).
- Qiao, B. et al. Highly efficient catalysis of preferential oxidation of CO in H₂-rich stream by gold single-atom catalysts. *ACS Catal.* **5**, 6249–6254 (2015).
- Kwak, J. H. et al. Coordinatively unsaturated Al³⁺ centers as binding sites for active catalyst phases of platinum on γ-Al₂O₃. *Science* **325**, 1670–1673 (2009).
- Wan, J. et al. Defect effects on TiO₂ nanosheets: stabilizing single atomic site Au and promoting catalytic properties. *Adv. Mater.* **30**, 1705369 (2018).
- Zhang, J. et al. Cation vacancy stabilization of single-atomic-site Pt₁/Ni(OH)_x catalyst for diboration of alkynes and alkenes. *Nat. Commun.* **9**, 1002 (2018).
- Wei, S. et al. Direct observation of noble metal nanoparticles transforming to thermally stable single atoms. *Nat. Nanotechnol.* **13**, 856–861 (2018).
- Fu, Q., Saltsburg, H. & Flytzani-Stephanopoulos, M. Active nonmetallic Au and Pt species on ceria-based water-gas shift catalysts. *Science* **301**, 935–938 (2003).
- Fu, Q., Deng, W., Saltsburg, H. & Flytzani-Stephanopoulos, M. Activity and stability of low-content gold–cerium oxide catalysts for the water–gas shift reaction. *Appl. Catal., B* **56**, 57–68 (2005).
- Hackett, S. F. J. et al. High-activity, single-site mesoporous Pd/Al₂O₃ catalysts for selective aerobic oxidation of allylic alcohols. *Angew. Chem., Int. Ed.* **46**, 8593–8596 (2007).
- Sun, S. et al. Single-atom catalysis using Pt/graphene achieved through atomic layer deposition. *Sci. Rep.* **3**, 1775 (2013).
- Zhang, S. et al. Catalysis on singly dispersed bimetallic sites. *Nat. Commun.* **6**, 7938 (2015).
- Gates, B. C., Flytzani-Stephanopoulos, M., Dixon, D. A. & Katz, A. Atomically dispersed supported metal catalysts: perspectives and suggestions for future research. *Catal. Sci. Technol.* **7**, 4259–4275 (2017).
- Liu, J. Catalysis by supported single metal atoms. *ACS Catal.* **7**, 34–59 (2016).
- Henrich, V. E. & Cox, P. A. *The surface Science of Metal Oxides*. (Cambridge University Press, Cambridge, 1994).
- DeRita, L. et al. Catalyst architecture for stable single atom dispersion enables site-specific spectroscopic and reactivity measurements of CO adsorbed to Pt atoms, oxidized Pt clusters, and metallic Pt clusters on TiO₂. *J. Am. Chem. Soc.* **139**, 14150–14165 (2017).
- Li, W. Z. et al. Stable platinum nanoparticles on specific MgAl₂O₄ spinel facets at high temperatures in oxidizing atmospheres. *Nat. Commun.* **4**, 2481 (2013).
- Bartholomew, C. H. Mechanisms of catalyst deactivation. *Appl. Catal., A* **212**, 17–60 (2001).
- Alcock, C. B. & Hooper, G. W. Thermodynamics of the gaseous oxides of the platinum-group metals. *Proc. R. Soc. Lond. Ser. A* **254**, 551–561 (1960).
- Carrillo, C. et al. Trapping of mobile Pt species by PdO nanoparticles under oxidizing conditions. *J. Phys. Chem. Lett.* **5**, 2089–2093 (2014).
- Ganzler, A. M. et al. Tuning the structure of platinum particles on ceria in situ for enhancing the catalytic performance of exhaust gas catalysts. *Angew. Chem. Int. Ed.* **56**, 13078–13082 (2017).
- Jones, J. et al. Thermally stable single-atom platinum-on-ceria catalysts via atom trapping. *Science* **353**, 150–154 (2016).
- Moliner, M. et al. Reversible transformation of Pt nanoparticles into single atoms inside high-silica chabazite zeolite. *J. Am. Chem. Soc.* **138**, 15743–15750 (2016).
- Xiong, H. et al. Thermally stable and regenerable platinum-tin clusters for propane dehydrogenation prepared by atom trapping on ceria. *Angew. Chem. Int. Ed.* **56**, 8986–8991 (2017).
- Xie, P. et al. Nanoceria-supported single-atom platinum catalysts for direct methane conversion. *ACS Catal.* **8**, 4044–4048 (2018).
- Nie, L. et al. Activation of surface lattice oxygen in single-atom Pt/CeO₂ for low-temperature CO oxidation. *Science* **358**, 1419–1423 (2017).
- Liu, X. et al. Strong metal-support interactions between gold nanoparticles and ZnO nanorods in CO oxidation. *J. Am. Chem. Soc.* **134**, 10251–10258 (2012).
- Qiao, B. et al. Ultrastable single-atom gold catalysts with strong covalent metal-support interaction (CMSI). *Nano Res.* **8**, 2913–2924 (2015).
- Liu, J.-C., Tang, Y., Wang, Y.-G., Zhang, T. & Li, J. Theoretical understanding of the stability of single-atom catalysts. *Natl. Sci. Rev.* **5**, 638–641 (2018).
- Liu, L. et al. Evolution and stabilization of subnanometric metal species in confined space by in situ TEM. *Nat. Commun.* **9**, 574 (2018).
- Ning, J. et al. Facile synthesis of magnetic metal (Mn, Fe, Co, and Ni) oxides nanocrystals via a cation-exchange reaction. *Nanoscale* **3**, 741–745 (2011).
- Sytnyk, M. et al. Tuning the magnetic properties of metal oxide nanocrystal heterostructures by cation exchange. *Nano. Lett.* **13**, 586–593 (2013).
- Hansen, T. W., DeLaRiva, A. T., Challa, S. R. & Datye, A. K. Sintering of catalytic nanoparticles: particle migration or ostwald ripening? *Acc. Chem. Res.* **46**, 1720–1730 (2013).
- Liu, J. C., Wang, Y. G. & Li, J. Toward rational design of oxide-supported single-atom catalysts: atomic dispersion of gold on ceria. *J. Am. Chem. Soc.* **139**, 6190–6199 (2017).
- Urfels, L., Gélin, P., Primet, M. & Tena, E. Complete oxidation of methane at low temperature over Pt catalysts supported on high surface area SnO₂. *Top. Catal.* **30**, 427–432 (2004).
- Zhai, Y. et al. Alkali-stabilized Pt-OH_x species catalyze low-temperature water-gas shift reactions. *Science* **329**, 1633–1636 (2010).
- Yang, M. et al. Catalytically active Au-O(OH)_x-species stabilized by alkali ions on zeolites and mesoporous oxides. *Science* **346**, 1498–1501 (2014).
- Yang, M. et al. A common single-site Pt(II)-O(OH)_x-species stabilized by sodium on “active” and “inert” supports catalyzes the water-gas shift reaction. *J. Am. Chem. Soc.* **137**, 3470–3473 (2015).
- Wei, H. et al. Remarkable effect of alkalis on the chemoselective hydrogenation of functionalized nitroarenes over high-loading Pt/FeO_x catalysts. *Chem. Sci.* **8**, 5126–5131 (2017).
- Wang, Y., Ren, J., Deng, K., Gui, L. & Tang, Y. Preparation of tractable platinum, rhodium, and ruthenium nanoclusters with small particle size in organic media. *Chem. Mater.* **12**, 1622–1627 (2000).
- Cui, Y. T. et al. Development of in-situ cell for fluorescence-mode XAFS in BL14B2 of Spring-8. *J. Phys. Conf. Ser.* **502**, 012039 (2014).
- Ravel, B. & Newville, M. ATHENA, ARTEMIS, HEPHAESTUS: data analysis for X-ray absorption spectroscopy using IFEFFIT. *J. Synchrotron Radiat.* **12**, 537–541 (2005).
- Kresse, G. & Joubert, D. From ultrasoft pseudopotentials to the projector augmented-wave method. *Phys. Rev. B: Condens. Matter Mater. Phys.* **59**, 1758–1775 (1999).

65. Kresse, G. & Furthmüller, J. Efficient iterative schemes for ab initio total-energy calculations using a plane-wave basis set. *Phys. Rev. B Condens. Matter Mater. Phys.* **54**, 11169–11186 (1996).
66. Perdew, J. P., Burke, K. & Ernzerhof, M. Generalized gradient approximation made simple. *Phys. Rev. Lett.* **77**, 3865–3868 (1996).
67. Anisimov, V. I., Aryasetiawan, F. & Lichtenstein, A. First-principles calculations of the electronic structure and spectra of strongly correlated systems: the LDA+*U* method. *J. Phys. Condens. Matter* **9**, 767–808 (1997).
68. Dudarev, S., Botton, G., Savrasov, S., Humphreys, C. & Sutton, A. Electron-energy-loss spectra and the structural stability of nickel oxide: An LSDA + *U* study. *Phys. Rev. B: Condens. Matter Mater. Phys.* **57**, 1505–1509 (1998).
69. Moses-DeBusk, M. et al. CO oxidation on supported single Pt atoms: experimental and ab initio density functional studies of CO interaction with Pt atom on theta-Al₂O₃(010) surface. *J. Am. Chem. Soc.* **135**, 12634–12645 (2013).
70. Narula, C. K. & Stocks, G. M. Ab Initio density functional calculations of adsorption of transition metal atoms on θ -Al₂O₃(010) surface. *J. Phys. Chem. C.* **116**, 5628–5636 (2012).

Acknowledgements

This paper is dedicated to the 70th anniversary of the Dalian Institute of Chemical Physics, Chinese Academy of Sciences. This work was supported by National Natural Science Foundation of China (21606222, 21573232, 21776270, 21590792, 91645203, 51761165012), National Key Projects for Fundamental Research and Development of China (2016YFA0202801, 2017YFA0700104), Strategic Priority Research Program of the Chinese Academy of Sciences (XDB17020100), and DNL Cooperation Fund, CAS (DNL180403). The synchrotron radiation experiment was performed at the BL14B2 of SPring-8 with the approval of Japan Synchrotron Radiation Research Institute (Proposal No. 2011B1974), Japan, and the BL14W1 at the Shanghai Synchrotron Radiation Facility, Shanghai Institute of Applied Physics, China. We thank Kratos Analytical Ltd, Manchester for LEIS measurements. Financial grant from the China Postdoctoral Science Foundation (2017M621170), DICP Outstanding Postdoctoral Foundation (2017YB02), and dedicated funds for methanol conversion from DICP. J. Luo thanks National Program for Thousand Young Talents of China, Tianjin Municipal Science and Technology Commission (15JCYBJC52600). The authors thank Kai Wang, Mengke Ge and Xingang Hou for their assistance with in situ STEM measurements. The computational work was performed using supercomputers at Tsinghua National Laboratory for Information Science and Technology and Lvliaing Tianhe-2 Supercomputing Center.

Author contributions

R.L. synthesized the catalyst and performed most of the reactions. S.M. performed the electron-microscopy characterization. W.X. and J.Luo performed the in situ electron microscopy. J.-C.L. and J.Li did the theoretical calculations and analysis. Y.-T.C., X.L. and Lei Li carried out the EXAFS experiment. Lin Li carried out the CO-DRIFT experiment. Y.C. and J.Lin provided reagent. T.L. and F.C. performed some experiments. A.F.L. provided the LEIS data and edited the manuscript. R.L. and B.Q. wrote the manuscript. A.-Q.W. and X.W. revised the paper. B.Q. and T.Z. designed the study and supervised the project.

Additional information

Supplementary Information accompanies this paper at <https://doi.org/10.1038/s41467-018-08136-3>.

Competing interests: The authors declare no competing interests.

Reprints and permission information is available online at <http://npg.nature.com/reprintsandpermissions/>

Journal peer review information: *Nature Communications* thanks the anonymous reviewers for their contribution to the peer review of this work. Peer reviewer reports are available.

Publisher's note: Springer Nature remains neutral with regard to jurisdictional claims in published maps and institutional affiliations.



Open Access This article is licensed under a Creative Commons Attribution 4.0 International License, which permits use, sharing, adaptation, distribution and reproduction in any medium or format, as long as you give appropriate credit to the original author(s) and the source, provide a link to the Creative Commons license, and indicate if changes were made. The images or other third party material in this article are included in the article's Creative Commons license, unless indicated otherwise in a credit line to the material. If material is not included in the article's Creative Commons license and your intended use is not permitted by statutory regulation or exceeds the permitted use, you will need to obtain permission directly from the copyright holder. To view a copy of this license, visit <http://creativecommons.org/licenses/by/4.0/>.

© The Author(s) 2019